Preprint: **Mean winds at the cloud top of Venus obtained from two-wavelength UV imaging by Akatsuki**

Submitted to the special issue of The Earth, Planets and Space: "Akatsuki at Venus: The First Year of Scientific Operation"

July, 2017

Mean winds at the cloud top of Venus obtained from two-wavelength UV imaging by Akatsuki

Takeshi Horinouchi (corresponding author), Faculty of Environmental Earth Science, Hokkaido University, N10W5, Sapporo, Hokkaido 060-0810, Japan, horinout@ees.hokudai.ac.jp (2nd affiliation: Institute of Space and Astronautical Science, Japan Aerospace Exploration Agency)
Toru Kouyama, Artificial Intelligence Research Center, National Institute of Advanced Industrial Science and Technology, t.kouyama@aist.go.jp
Yeon Joo Lee, Institute of Space and Astronautical Science, Japan Aerospace Exploration Agency, leeyj@ac.jaxa.jp
Shin-ya Murakami, Institute of Space and Astronautical Science, Japan Aerospace Exploration Agency, murashin@gfd-dennou.org
Kazunori Ogohara, School of Engineering, University of Shiga Prefecture, ogohara.k@e.usp.ac.jp
Masahiro Takagi, Division of Science, Kyoto Sangyo University, takagi.masahiro@cc.kyoto-su.ac.jp
Takeshi Imamura, Graduate School of Frontier Sciences, the University of Tokyo, t_imamura@edu.k.u-tokyo.ac.jp
Kensuke Nakajima, Graduate School of Sciences, Kyushu University, kensuke@geo.kyushu-u.ac.jp
Javier Peralta, Institute of Space and Astronautical Science, Japan Aerospace Exploration Agency, javier.peralta@ac.jaxa.jp
Atsushi Yamazaki, Institute of Space and Astronautical Science, Japan Aerospace Exploration Agency, yamazaki@stp.isas.jaxa.jp
Manabu Yamada, Planetary Exploration Research Center, Chiba Institute of Technology, manabu@perc.it-chiba.ac.jp
Shigeto Watanabe, Space Information Center, Hokkaido Information University, space.shw.s@gmail.com

Abstract

Venus is covered with thick clouds, and ultraviolet (UV) images at 0.3—0.4 μm, at which an unknown UV absorbing substance allows to visualize cloud features, have been used to estimate winds at the cloud top level situated at ~70 km above the mean surface. In this study, we report low-latitude winds obtained from the images taken by the UV imager, UVI, onboard Akatsuki orbiter from December 2015 to March 2017. UVI provides images with two filters centered at 365 and 283 nm. While the 365-nm images enable to continue the traditional Venus observations, the 283-nm images visualize cloud features at an SO_2 absorption band, which is novel. We used a sophisticate automated cloud tracking method and elaborate quality control to estimate winds with high precision. Horizontal winds obtained from the 283-nm images are generally similar to those from the 365-nm images, but in many cases, westward winds from the former are faster than the latter by a few m/s. From previous studies, one can argue that the 283-nm images are likely to reflect cloud features at higher altitude than the 365-nm images. If it is the case, the superrotation of Venusian atmosphere is generally increased with height even at the cloud-top level, where it has been thought that it is roughly peaked. The mean winds obtained from the 365-nm images exhibit local-time dependence consistent with the tidal features reported earlier. A previous study suggested that the geographic distribution of temporal mean zonal winds obtained from UV images from Venus Express orbiter over 2006—2012 can be interpreted as forced by topographically induced

stationary gravity waves. However, the geographic distribution of temporal mean zonal winds we obtained is qualitatively different from that distribution, suggesting that the distribution may not be persistent.

Keywords

Venus, Planetary atmosphere, Planetary climatology, Cloud tracking, Image velocimetry, Superrotation, Aerosol, Wind shear, Cloud motion vector, SO2

Introduction

Venus is covered with thick clouds that extend from ~45 to ~70 km altitude above the mean surface. Ultraviolet (UV) images at around 0.3—0.4 μm of the dayside of Venus exhibit remarkable contrast owing to a UV absorbing substance that has not been identified (Pollack et al., 1980; Esposito et al., 1997). Small-scale features at the cloud top captured by UV images have been extensively used for cloud tracking (e.g., Limaye and Suomi, 1981; Limaye et al. 1982, 1988; Rossow et al, 1990; Toigo et al 1994; Peralta et al. 2007; Moissl et al. 2009; Sánchez-Lavega et al 2009; Kouyama et al 2012, 2013; Khatuntsev et al, 2013; Hueso et al. 2015; Peralta et al. 2017). These studies are based on planetary exploration with Mariner 10, Pioneer Venus Orbiter (PVO), Galileo, Venus Express (VEx), and Messenger and have revealed the meridional structure of the superrotation, significant motion associated with the

68 thermal tide, long-term variability of mean winds, and the existence and the variability of
69 planetary-scale waves (Kelvin and Rossby waves). Because of the long-term variability found
70 in mean winds and wave activity (Rossow et al. 1990; Khatuntsev et al. 2013; Kouyama et al.
71 2013, extension with new observations is of great interest.

72 Akatsuki spacecraft was launched in 2010, and five years after the failure of orbital
73 insertion in the same year, it was maneuvered to start orbiting Venus on Dec 7, 2015
74 (Nakamura et al 2016). Its present orbital period is about 11 days, and its low orbital
75 inclination (<10°) makes it suitable to observe low latitude. Akatsuki is equipped with
76 cameras to observe Venus at multiple wavelengths. In this study, we use data from one of
77 them, the Ultraviolet Imager, UVI. UVI images Venus with two filters centered at 365 nm and
78 283 nm (Yamazaki et al 2017). With the 365-nm filter, UVI provides images equivalent to
79 those from the previous missions listed above; in other words, it provides cloud images
80 contrasted by the unknown UV absorber. On the other hand, the 283-nm filter is designed to
81 match an SO_2 absorption band.

82 Before Akatsuki, spacecraft observations of Venus at SO_2 absorption bands were conducted
83 only by PVO, which has a spectrometer that covers the two broad SO_2 absorption bands
84 around 210 nm and 280 nm. To the authors' knowledge, Limaye (1984) is the only study that
85 utilized an SO_2 absorption band for cloud tracking, where he used polarization features, not
86 the intensity contrasts as in the above mentioned studies. Among the four wavelengths he

used (270, 365, 550, 935 nm), the 270-nm polarization features suggested the fastest westward wind speed. However, his result at 365-nm is much slower than the intensity-based results at this wavelengths, which suggests that his results might have a large error. Therefore, it would be interesting to update the wavelength dependence by using data from Akatsuki.

The purpose of this study is to report the initial results of cloud tracking by using UVI images. After introducing a case study to show the overall performance at both wavelengths, we focus on mean winds and the similarity and the difference of winds obtained at the two-wavelengths by using data over a year and four months. In this initial study, we limit our scope between 50°S and 50°N, and we mainly focus on low latitude. Cloud tracking with UVI is more difficult for high-latitude due to Akatsuki's equatorial orbit and because UV cloud features at mid-to-high latitude exhibit as featureless streaks (Rossow et al. 1980, Titov et al. 2012). Therefore, to study flow at high latitude is left for future study.

Data and Method

We used the version 20170601 Level-3 UVI data covering the period from December 7, 2015 to March 25, 2017, in which 3,231 images are available. The level-3 data consist of radiance mapped onto a longitude-latitude grid with a resolution of 0.125° both in longitude and latitude as described by Ogohara et al. (2012).

106 We conducted cloud tracking by using a novel automated method by Ikegawa and
107 Horinouchi (2016; hereinafter IH16) and Horinouchi et al. (2017a; hereinafter H17a). The
108 method is based on the traditional template matching in which cross-correlation peaks are
109 searched (e.g, Limaye 1981; Kouyama et al 2012), but it can utilize multiple (more than two)
110 images consistently to accurately estimate horizontal winds (IH16). The method also supports
111 a sophisticated error correction with the relaxation labeling technique, which is similar to the
112 one used by Kouyama et al (2012) but is significantly improved (H17a). The parameter setting
113 is the same as in Horinouchi et al (2017b): the template size is 7.5° both in longitude and
114 latitude; horizontal winds are obtained at grid points with a 3° interval; and we employed the
115 spatial sliding average of cross-correlation surfaces at adjacent grid points (center plus the
116 four upper/lower/left/right ones, which is called the "STS" type setting in IH16). See the
117 Method section (online supplement) of Horinouchi (2017b) for further details in addition to the
118 method description in IH16 and H17a. Horizontal wind data obtained by cloud tracking are
119 often called as cloud motion vectors (CMVs), so we sometimes use this abbreviation in what
120 follows for brevity.
121 When Akatsuki's geometry of observations is favorable for the dayside of Venus, UVI is
122 operated to conduct a sequence of 283- and 365-nm imaging at a time interval of ~3 minutes.
123 Normally, this sequence is repeated every two hours during several to 16 hours; imaging is not
124 continued over a full day because the attitude of the spacecraft needs to be altered for data

125 transfer to the Earth.

126 Cloud tracking is conducted for all available two-hourly image triplets over four hours for
127 each of the two wavelengths. In other words, if the UVI imaging sequence is conducted at 10,
128 12, 14,…, 22 hours in a day, we conducted cloud tracking by using the images at 10—12—14,
129 12—14—16,…, 18—20—22 hours, which provides five CMV datasets for each wavelength.
130 Exceptionally, we used images with slightly longer time intervals on December 7, 2015, as
131 introduced in the next section. In the Akatsuki L3 data, the camera boresight orientation data
132 are corrected with a limb-fitting technique (Ogohara et al., 2012). We did not use images for
133 which the fitting was unsuccessful, which occurs mainly when the spacecraft is near Venus
134 and the limb is captured only partially.

135 The period of our observations cover from December 7, 2015 to March 25, 2017 (475 days),
136 with UVI acquiring images during a total of 295 days. We obtained cloud tracking results from
137 1,034 365-nm image triplets in 193 days and 1,039 283-nm image triplets in 195 days;
138 observational condition in the other 100 days was unsuitable for the tracking using three
139 two-hourly images.

140 As a quality control, derived CMVs are screened to retain only those associated with the
141 cross-correlation coefficient higher than 0.5 and the precision measure, termed ε in IH16,
142 smaller than 10 m/s. We also adapted the screening to satisfy the “deformation consistency”
143 principle as proposed by H17a (see their section 5.1). In the **Mean Winds** section, the

144 threshold of ε is set to 20 m/s for initial screening, and later, further screening based on ε
145 statistics is conducted as will be described there. Also, when computing the mean quantities
146 shown the section, CMVs associated with the template region where satellite zenith angle is
147 greater than 60° are excluded; this is to cope with possible small error in camera parameters
148 that may need further optimization.

149 The precision in the measurements is actually defined separately for zonal and meridional
150 winds, which are referred to as ε_u and ε_v, respectively (IH16); ε is simply the greater of the
151 two.

152

153 **Case Study**

154 Here we show the results from UVI images obtained on December 7, 2015, which is the
155 first day of Akatsuki's observation. The UVI imaging on the day was conducted at 5, 17, 20,
156 and 22 h UTC, so tracking was conducted with the last three. Venus's diameter in the images
157 is ~380 pix at 17 h and ~320 pix at 22 h, corresponding to the resolution at the sub-spacecraft
158 point 30 to 40 km. During the five hours, the sub-solar longitude moved eastward by 0.6° from
159 143.0°, and the sub-spacecraft longitude moved westward by 2° from 82.5°.

160 **Figure 1a** shows the horizontal winds obtained from the 365-nm images. Since the flow is
161 dominated by the superrotation, we show by arrows the deviation from the solid-body rotation
162 whose westward speed is 100 m/s at the equator (i.e., $[u + 100\cos\varphi, v]$ m/s, where u and v

163 are zonal and meridional velocity, and φ is latitude). The movement of hypothetical tracers
164 advected linearly with time by the derived winds (shown by the cross marks in **Fig. 1a—c**) has
165 a good correspondence with the movement of small-scale (~several hundred km) radiance
166 features, suggesting the appropriateness of our result. Here, the radiance is band-pass filtered
167 by applying the Gaussian filters with the half-widths at half-maximum of 4° (high-pass) and
168 0.3° (low-pass) with both longitude and latitude.

169 The flow field shown in **Figure 1a** exhibits zonal and meridional divergence consistent with
170 the tidal features at the cloud top level shown by previous studies (e.g., Limaye 1988; Del
171 Genio and Rossow, 1990; Khatuntsev et al, 2013). This snapshot-flow field is much smoother
172 than those reported in earlier studies (e.g., Limaye 1981; Kouyama et al 2012) except IH16. It
173 is probably the first time to show the tidal feature in a snapshot. The smoothness is partly due
174 to the overlap of template regions (while the template regions size is 7.5°, CMV grid points are
175 taken at a 3° interval, and a sliding average is applied to cross-correlation surfaces), but note
176 that no smoothing is applied to derived winds.

177 Perhaps more interesting results would be the ones obtained from the images at 283-nm,
178 an SO_2 absorption band, at which only Limaye (1984) reported tracking results (see
179 **Introduction**). **Figure 2** shows the result from the 283-nm images taken almost
180 simultaneously with the 365-nm images shown in **Fig. 1.** Small-scale features are similar
181 between the two wavelengths; the cross-correlation of the band-pass results are 0.73 over the

three image pairs shown in the figures, which indicates that a half of the variances on the shown scale are in common between the two wavelengths ($0.73^2 = 0.53$).

As expected from the correlation, the wind estimates at the two wavelengths shown in **Figs. 1** and **2** generally agree well with each other, but 283-nm winds often exhibit faster westward speeds. **Figure 3** shows the close-up of the latitudinal range of 13°S to 7°S for close inspection. Winds from the two filters agree better with each other in the eastern half than in the western half of the region shown. Also, the radiance features agree well between the two filters in the eastern regions. In the western region, feature agreement between the two filters is weaker. Furthermore, although we can roughly follow the movement of features at the velocities derived for each filter, the traceability is not good at everywhere, and it appears that the temporal change of radiance features is not always described by simple advection. Inspection of many UVI images sometimes suggests hints of superposed multiple velocities (not shown). This aspect will be investigated further in a future study.

Figure 4 summarizes the wind estimates for December 7, 2015. Note that the precision estimates (stippled where ε_u or ε_v is smaller than 4 m/s) tends to be better (i.e., smaller) in the eastern half of the region shown in **Fig. 3**. The area of stippled region in **Fig. 4b** is smaller than in **Fig. 4a**, which is consistent with the fact that 283-nm images are noisier than 365-nm images.

Overall differences between 283- and 365nm results

We now turn to long-term statistics. **Figure 5** shows the difference between the winds obtained at the two wavelengths (283-nm results minus 365-nm results) averaged over the observation period. It is obtained by selecting simultaneous tracking results at two wavelengths, finding grid points where the CMVs passed the screening at both wavelengths, and averaging their differences with longitude and time. The result suggests that the westward winds obtained with 283-nm images are faster than those from 365-nm images on the average; the mean difference is 2—4 m/s. In total, 77% of the differences used to make **Fig. 5a** are negative. On the other hand, the differences in meridional winds are not clear. The difference is further explored in what follows.

Mean Winds

Here we show mean winds obtained from the entire analysis period (December 2015 to March 2017). All the quantities shown in this section are derived from the daily mean values derived as in what follows. Observation time for consecutive UVI imaging is typically over a half day, but it varies significantly day by day. Therefore, to avoid uneven weighting depending on the observation hours, zonal and meridional winds are first averaged for each day (based on UTC) at each geographical (longitude-latitude) grid points. As for the precision measures ε_u and ε_v, their daily values are defined as $\bar{\varepsilon_x} \equiv \sqrt{\sum_{i=1}^{n} \varepsilon_x^2}/n$ instead of averaging,

where x represents u or v, and n is the number of the valid data in each day at each grid point; here, the valid data indicate those that passed the screening stated in the **Method and Data** section. The above definition of $\bar{\varepsilon}_x$ is suitable to treat random errors. Where long-term mean is shown, they are further summed as

$$\langle \varepsilon_x \rangle \equiv \sqrt{\sum_{i=1}^{N} \bar{\varepsilon}_x^2} / N \qquad (x \text{ represents } u \text{ or } v) \tag{1}$$

where N is the number of daily values used to compute the long-term mean at each grid point (whether on longitude–latitude or local time–latitude grid).

The long-term mean zonal and meridional winds are shown with respect to local time and longitude in **Figure 6**. The 365-nm results (**Fig. 6a,b**) are consistent with previous studies (e.g., Limaye 1988; Del Genio and Rossow, 1990; Moissl, 2009; Khatuntsev et al, 2013; Hueso et al. 2015). Namely, dayside zonal wind at low-latitude is slowest around the longitude corresponding to the local noon, and meridional wind divergence is the strong in the early to mid afternoon. Quantitatively, it appears that our result is closer to the ones obtained from PVO (Limaye 1988; Del Genio and Rossow, 1990) and VEx/VIRTIS (Hueso et al. 2015) rather than those by VEx/VMC (Moissl, 2009; Khatuntsev et al, 2013); for instance, the westward wind minimum is located slightly in the morning side of the longitude of local noon. However, it should be noted that the tidal structure may be subject to long-term variability, and that its statistics may be affected by the partial sampling that arises from the use of a single satellite, as explained in what follows.

239 The values obtained for $\langle \varepsilon_u \rangle$ and $\langle \varepsilon_v \rangle$ are rather small at low latitude, indicating good
240 precision; stipples in **Fig. 6** show where their values are smaller than 4 m/s. However, it
241 should be reminded that they do not include any effect of biases that arise from limited
242 sampling. The time coverage of 365-nm tracking result can be seen in **Fig. 7a**, which shows
243 5-day mean zonal winds between 20°S and 20°N. The around-the-noon maxima (minima in
244 terms of wind speed) stated above can be seen at most of the times. However, a long-term
245 variability seems apparent over time scales of O(100) days, as suggested by Kouyama et al
246 (2013) and Khatuntsev et al. (2013). **Figure 7a** implies that such a long-term variability can be
247 aliased into the local-time dependence shown in **Fig. 6** through the slowly moving
248 observational local-time window. Note that the observational window is associated with the
249 spacecraft's orbit; although Akatsuki takes a low-inclination orbit, imaging suitable for cloud
250 tracking is conducted mainly for the hemisphere around the apoapsis longitude, since the
251 orbit is highly elliptic (Nakamura et al, 2016). The apoapsis longitude moves as Venus rotates
252 at the period of 243 days. Similar observational windows exist for the past orbiters too.
253 **Figures 6** and **7** show that the westward winds obtained from 283-nm images are
254 consistently faster than those from 365-nm images at all time. On the other hand, meridional
255 winds show good agreement within the expected precision (**Fig. 6b,d**).
256 Bertaux et al (2016) suggested the existence of longitudinal dependence in mean zonal
257 winds. For comparison, we made similar statistics. **Figures 8a** shows the temporal-mean zonal

wind averaged simply at each longitudinal and latitudinal grid point. It exhibits a large-longitudinal variation. However, **Fig 7c** suggests that the observational time coverage is quite limited for each longitude. Furthermore, there is no clear longitudinally-fixed structure that persists over the observational period. Comparison of **Fig. 7a** and **c** indicates that local time dependence is more robust. Therefore, we show in **Fig. 8b** the temporal-mean zonal winds in which the local time dependence is subtracted, even though the latter is also not free from biases due to the partial sampling (as mentioned above). It was computed as follows: firstly, the local time dependence was obtained by subtracting from the local-time dependent mean winds (as shown in **Fig. 6**) their zonal mean; then, the local time dependence is subtracted from the daily-mean zonal winds; and finally the result was averaged over the observational period.

As expected, mean zonal winds shown in **Fig. 8b** exhibits smaller longitudinal variation than in **Fig. 8a**. However, they are qualitatively similar. The longitudinal dependence we obtained does not agree with that shown by Bertaux et al. (2016) even qualitatively. Specifically, they showed that low-latitudinal westward winds in the eastern hemisphere (0—180°) is slower than those in the western hemisphere. The hemispheric contrast indicated by **Fig. 8b** (as well as **Fig. 8a**) is opposite. We do not insist that **Fig. 8b** represent true geographic dependence, but it is interesting that the geographic dependence shown by Bertaux et al. (2016) may not be present all the time.

Discussion

What causes the difference in the zonal winds obtained from the 283- and 365-nm images? A possible explanation is that when the velocities disagree, small-scale features at the two wavelengths reflect clouds at different heights, so the difference is from vertical shear. Another possibility is that while the velocity captured at one wavelength represents the flow velocity, the velocity captured at the other wavelength represents the phase velocity of atmospheric waves. A close inspection suggests that it indeed appears the case sometimes, but in most cases, it appears unlikely. For the spatial scale of our template (7.5°, i.e. about 800 km), the kind of atmospheric waves that should be considered is the gravity waves, since the intrinsic phase velocity of small-scale Rossby waves is too slow to distinguish from flows unless strong local beta effect exists and sound waves are clearly irrelevant. However, in many cases, we do not see clear wavy features. The fact that the velocity difference is mainly in the zonal direction indicates that if it is explained by waves, the constant phase lines should be predominantly in the north-south direction. However, we do not see such anisotropy evidently. Therefore, we can conclude that the overall difference is likely due to vertical shear.

Then the next question that arises is which of the two represents the flow at higher altitude. Previous studies that derived thermally balanced zonal winds from radio occultation observations suggested that the zonal wind speeds are peaked roughly at around 70 km where

296 cloud top resides (e.g., Limaye, 1985; Piccialli et al., 2012). However, the thermal wind
297 derivation has large uncertainty at low latitude. Studies with entry probe observations have
298 shown the vertical structure of zonal winds at low latitude, but large uncertainty exists above
299 65 km (Schubert et al., 1980; Kerzhanovich and Limaye, 1985). Therefore, it is difficult to tell
300 whether the faster represent flow at the higher or the lower altitude from these studies. In a
301 recent work, Peralta et al. (2017) estimated the vertical profile of the zonal winds during the
302 second Venus flyby of NASA's Messenger spacecraft, and the results suggested that on the
303 dayside the altitude at which the zonal wind peaks seems variable with time. However, it is a
304 case study.

305 A clue to the question is found in the estimated vertical distributions of absorbers. Lee et
306 al (2017) found that the phase-angle dependency in Akatsuki UVI 365-nm data can be
307 explained if the unknown absorber is distributed slightly below cloud top rather than above.
308 On the other hand, SO_2 mixing ratio increases upward from the clouds top level (e.g., Belyaev,
309 2012; Mahieux et al. 2015). Therefore we speculate that the motion obtained from 283-nm
310 images reflect flows at higher altitude. However, further study would be needed to verify it,
311 since SO_2 density has a strong downward gradient in the cloud layer (e.g., von Zahn et al.,
312 1983).

313 Another point of issue to discuss is the discrepancy between our results and Bertaux et al.
314 (2016) in terms of geographic distribution of temporal mean zonal winds. Bertaux et al. (2016)

315 used observations over a longer period (7.5 years) than ours (1.3 years). In that sense, their
316 result appears more reliable. However, the longitudinal variation they showed is greater than
317 our result shown in **Fig. 8b**, so we cannot say *a priori* that the expected sampling error is
318 smaller in their study than in ours. They interpreted their geographic distribution as a result
319 of the deceleration by topographically induced gravity waves that propagate from the ground.
320 However, the longitudinal distribution of momentum forcing does not necessarily induce such
321 features, as is evident from the quasi-biennial oscillation (QBO) in the equatorial stratosphere
322 of the Earth. Even though the driving force of the QBO is known to have significant
323 longitudinal asymmetry, the equatorial zonal wind has longitudinal variation much smaller
324 than that shown by Bertaux et al. (2016) (Kawatani et al, 2005, 2010). To solve the geographic
325 distribution mystery would require further study.
326
327 **Summary and conclusions**
328 We have estimated and investigated winds at the cloud top of Venus by using UV images
329 obtained by UVI onboard Akatsuki. The novel automated cloud-tracking method and the
330 quality control proposed by IH16 and H17a enabled us to obtain realistic winds that actually
331 reflect the motion of small-scale features at the wavelengths of 365 and 283 nm, the
332 traditional UV imaging based on the unknown UV absorber and the novel UV imaging at an
333 SO_2 absorption band, respectively.

Horizontal winds obtained from the 283-nm images are generally similar to those from the 365-nm images, but in many cases, zonal winds from the former are faster than the latter. It was suggested that the difference is associated with vertical wind shear. From the studies of Lee et al. (2017) and others, one can argue that 283-nm images are expected to reflect cloud features at higher altitude than 365-nm images. Therefore, we can tentatively conclude that, on the average, it is likely that the superrotation of Venusian atmosphere is increased with height even at the cloud-top level, where previous studies suggested that the zonal wind speeds are roughly maximized.

We derived mean winds averaged over the observation period as functions of local time and latitude. The result is consistent with previous studies, which have shown the wind structures associated with the thermal tide. Furthermore, the local-time—time plots of low-latitude zonal winds suggested a hint of long-term variability. It should be noted, however, that the long-term variability can be aliased into the local-time–latitude map of mean winds. This problem may be alleviated by using simultaneous ground-based observation from the Earth. Also, the tidal structure may vary slowly with time. Further study would be needed to improve our knowledge on the thermal tide in the atmosphere of Venus.

Bertaux et al (2016) obtained the geographical distribution of temporal mean zonal winds using UV images from VEx, and they suggested that it is explained as a result of the forcing by topographically induced stationary gravity waves. However, the geographical distribution

353 we obtained is qualitatively different from theirs. This result indicates that the distribution
354 they showed may not be persistent. Further study would be needed to draw a firm conclusion
355 on this issue.
356
357 **Acknowledgement**
358 We thank Drs. Takehiko Sato, Sanjay Limaye, Masato Nakamura, and Hiroki Kashimura
359 for discussion on UVI tracking results. We also thank the numerous people who contributed to
360 create and operate Akastuki spacecraft. This study is partially supported by JSPS KENHI
361 16H02231 and16H02225 and JAXA's ITYF Fellowship.
362
363 **References**
364 Belyaev, D. A., Montmessin, F., Bertaux, J. L., Mahieux, A., Fedorova, A. A., Korablev, O. I. &
365 Zhang, X. (2012). Vertical profiling of SO 2 and SO above Venus' clouds by SPICAV/SOIR
366 solar occultations. *Icarus*, 217(2), 740-751.
367 Bertaux, J. L., Khatuntsev, I. V., Hauchecorne, A., Markiewicz, W. J., Marcq, E., Lebonnois, S.,
368 Patsaeva, M. Turin, A., & Fedorova, A. (2016). Influence of Venus topography on the zonal
369 wind and UV albedo at cloud top level: The role of stationary gravity waves. Journal of
370 Geophysical Research: Planets, 121(6), 1087-1101.
371 Del Genio, A. D., & W. B. Rossow, (1990). Planetary-scale waves and the cyclic nature of cloud

372 top dynamics on Venus. Journal of the Atmospheric Sciences, 47(3), 293-318.

373 Esposito, L. W., Bertaux, J. L., Krasnopolsky, V. L. A. D. I. M. I. R., Moroz, V. I., & Zasova, L. V.

374 (1997). Chemistry of lower atmosphere and clouds. *Venus II*, University of Arizona Press ,

375 415-458.

376 Horinouchi, T., S. Murakami T. Kouyama, K. Ogohara, A. Yamazaki, M. Yamada, and S.

377 Watanabe (2017a) Image velocimetry for clouds with relaxation labeling based on

378 deformation consistency. *Measurement Science and Technology*, in press. Doi:

379 https://doi.org/10.1088/1361-6501/aa695c.

380 Horinouchi, T. et al (2017b) Equatorial jet in the lower to middle cloud layer of Venus revealed

381 by Akatsuki. *Nature Geoscience*, submitted.

382 Ikegawa, S., & T. Horinouchi (2016) Improved automatic estimation of winds at the cloud top

383 of Venus using superposition of cross-correlation surfaces. *Icarus*, 271, 98-119.

384 Hueso, R., Peralta, J., Garate-Lopez, I., Bandos, T. V. & Sánchez-Lavega, A. Six years of Venus

385 winds at the upper cloud level from UV, visible and near infrared observations from VIRTIS on

386 Venus Express. *Planet. Space Sci.* **113-114**, 78–99 (2015).

387 Kawatani, Y., K. Tsuji, & M. Takahashi (2005) Zonally non - uniform distribution of

388 equatorial gravity waves in an atmospheric general circulation model. *Geophys. Res. Lett.*,

389 32(23).

390 Kawatani, Y., S. Watanabe, K. Sato, T. J. Dunkerton, S. Miyahara, & M. Takahashi, (2010)

391 The roles of equatorial trapped waves and internal inertia–gravity waves in driving the
392 quasi-biennial oscillation. Part II: Three-dimensional distribution of wave forcing. *J. Atmos.*
393 *Sci.*, 67(4), 981-997.
394 Kerzhanovich, V. V., & S. S. Limaye (1985). Circulation of the atmosphere from the surface to
395 100 km. *Advances in Space Research*, 5(11), 59-83.
396 Khatuntsev, I. V., Patsaeva, M. V., Titov, D. V., Ignatiev, N. I., Turin, A. V., Limaye, S. S.,
397 Markiewicz W.J., Almeida, M. Roatsch, Th. & Moissl, R. (2013). Cloud level winds from the
398 Venus Express Monitoring Camera imaging. Icarus, 226(1), 140-158.
399 Kouyama, T., T. Imamura, M. Nakamura, T. Satoh, & Y. Futaana (2012) Horizontal structure
400 of planetary-scale waves at the cloud top of Venus deduced from Galileo SSI images with an
401 improved cloud-tracking technique. *Planetary and Space Science*, 60(1), 207-216.
402 Kouyama, T, T. Imamura, M. Nakamura, T. Satoh, & Y. Futaana (2013) Long - term variation
403 in the cloud - tracked zonal velocities at the cloud top of Venus deduced from Venus
404 Express VMC images. *J. Geophys. Res. (Planets)*, 118(1), 37-46.
405 Lee, Y. J., A. Yamazaki, T. Imamura, M. Yamada, S. Watanabe, T. M. Sato, K. Ogohara, G. L.
406 Hashimoto, and S. Murakami (2017) Scattering properties of the Venusian clouds observed
407 by UV Imager on board Akatsuki. *Astronomical Journal*, accepted.
408 Limaye S. S., and V. E. Suomi (1981) Cloud motions on venus: Global structure and
409 organization. *J. Atmos. Sci.*, 38(6), 1220-1235.

410 Limaye, S. S., C. J. Grund, & S. P. Burre (1982) Zonal mean circulation at the cloud level on
411 Venus: Spring and Fall 1979 OCPP observations. *Icarus*, 51(2), 416-439.
412 Limaye, S. S. (1984) Morphology and movements of polarization features on Venus as seen in
413 the Pioneer Orbiter Cloud Photopolarimeter data. *Icarus*, 57, 362—385.
414 Limaye, S. S. (1985) Venus atmospheric circulation: Observations and implications of the
415 thermal structure. *Advances in Space Research*, 5(9), 51-62.
416 Limaye, S.S., Grassotti, Ch., Kuetemeyer, M.J., (1988) Venus: Cloud level circulation during
417 1982 as determined from Pioneer Cloud Photopolarimeter images. I. Time and zonally
418 averaged circulation. *Icarus* 73, 193–211.
419 Limaye, S.S., 1988. Venus: Cloud level circulation during 1982 as determined from Pioneer
420 Cloud Polarimeter images. II. Solar longitude dependent circulation. *Icarus* 73, 212–226.
421 Mahieux, A., Vandaele, A. C., Robert, S., Wilquet, V., Drummond, R., Chamberlain, S., Belyaev,
422 D., & Bertaux, J. L. (2015). Venus mesospheric sulfur dioxide measurement retrieved from
423 SOIR on board Venus Express. Planetary and Space Science, 113, 193-204.
424 Moissl, R., et al. (2009) Venus cloud top winds from tracking UV features in Venus Monitoring
425 Camera images. *J. Geophys. Res. (Planets)*, 114, E00B31. DOI: 10.1029/2008JE003117.
426 Nakamura, M. et al. (2016) AKATSUKI returns to Venus. *Earth Planets Space*, 68—75,
427 doi:10.1186/s40623-016-0457-6.
428 Ogohara, K., et al. (2012) Automated cloud tracking system for the Akatsuki Venus Climate

Orbiter data. *Icarus*, 217, 661—668, doi:10.1016/j.icarus.2011.05.017.

Peralta, J., R. Huseo, A. Sanchez-Lavega (2007) Areanalysis of Venus winds at two cloud levels from Galileo SSI images. *Icarus*, 190, 469-477.

Peralta, J., Lee, Y. J., Hueso, R., Clancy, R., Sandor, B., Sánchez-Lavega, A., Lellouch, E., Rengel, M., Machado, P., Omino, M., Piccialli, A., Imamura, T., Horinouchi, T., Murakami, S., Ogohara, K., Luz, D. & Peach D. Venus's Winds and Temperatures during the Messenger's flyby: an approximation to a three-dimensional instantaneous state of the atmosphere. *Geophys. Res. Lett.* **44**, 3907-3915 (2017).

Piccialli, A., Tellmann, S., Titov, D. V., Limaye, S. S., Khatuntsev, I. V., Pätzold, M., & Häusler, B. (2012) Dynamical properties of the Venus mesosphere from the radio-occultation experiment VeRa onboard Venus Express. *Icarus*, 217(2), 669-681.

Pollack, J. B., Toon, O. B., Whitten, R. C., Boese, R., Ragent, B., Tomasko, M., Esposite, L., Travis, L.,& Wiedman, D. (1980). Distribution and source of the UV absorption in Venus' atmosphere. *J. Geophys. Res.*, 85(A13), 8141-8150.

Rossow, W. B., A. D. Del Genio, S. S. Limaye, L. D. Travis, & P. H. Stone (1980) Cloud morphology and motions from Pioneer Venus images. *J. Geophys. Res.*, 85(A13), 8107—8128.

Rossow, W. B., A. D. del Genio, and T. Eichler, Cloud-tracked winds from Pioneer Venus OCPP images, *J. Atmos. Sci.*, 47, 17, 2053-2084, 1990.

448 Sánchez - Lavega, A. et al. (2008) Variable winds on Venus mapped in three dimensions.
449 *Geophys. Res. Lett.*, 35(13), doi:10.1029/2008GL033817.
450 Schubert, G., et al. (1980) Structure and circulation of the Venus atmosphere. *J. Geophys. Res.*,
451 85(A13), 8007—8025.
452 Titov, D. V. et al. Morphology of the cloud tops as observed by the Venus Express Monitoring
453 Camera. *Icarus* **217**, 682-701 (2012).
454 Toigo, A., P.J.Gierasch, & M.D. Smit (1994) High resolution cloud feature tracking on Venus
455 by Galileo. *Icarus*, 109, 318–336.
456 von Zahn, U., Kumar, S., Niemann, H., & Prinn, R. (1983) Composition of the Venus
457 atmosphere. *Venus*, University of Arizona Press, Ch.13, 299-430.
458 Yamazaki, A. et al (2017) Ultraviolet Imager on Venus Climate Orbiter, Akatsuki and its
459 initial results. Submitted to the Akatsuki special issue of *Earth Planets Space*.
460

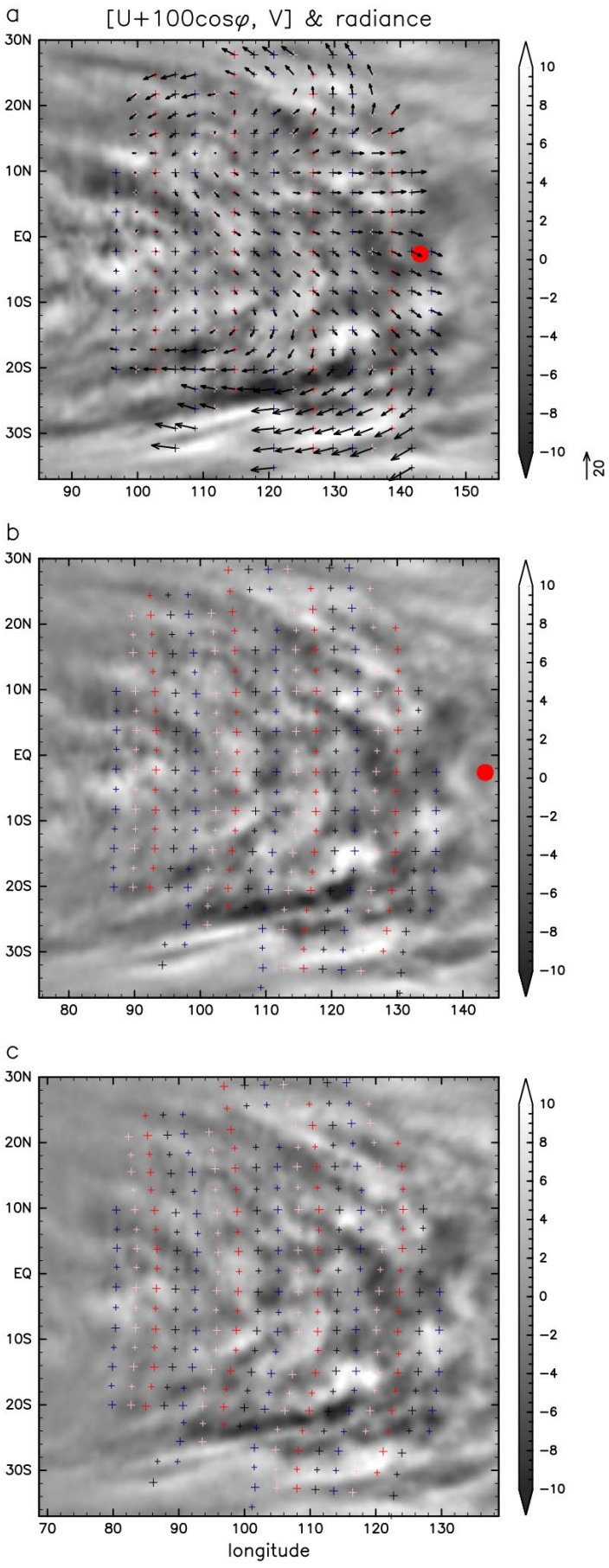

Figure 1: Band-pass filtered 365-nm radiance and cloud tracking results for December 7, 2015. Gray-scale shading shows the filtered radiance at (a) 17:29, (b) 20:19, and (c) 22:19 UTC used for the tracking (W m^{-2} sr^{-1} μm^{-1}). Arrows (a) show the horizontal wind deviation from the solid-body rotation whose westward speed is 100 m/s at the equator. The longitude (abscissa) ranges of the three panels are adjusted to compensate the solid-body rotation. Colored "+" symbols at the initial time (a) show the centers of the template regions for cloud tracking, while those at later times (b, c) show their positions advected linearly with time by the CMVs. Red bullets indicate the sub-solar point.

461

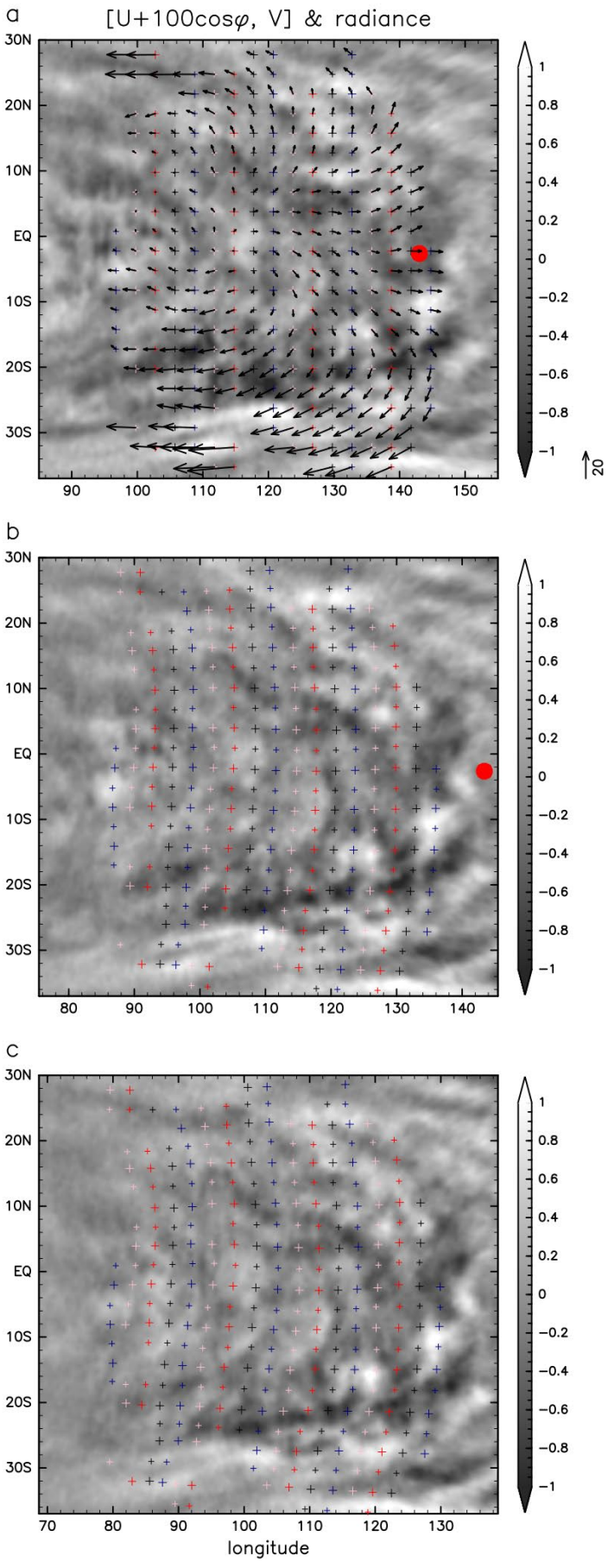

Figure 2: As in **Figure 1** but for showing the results from 283-nm radiance obtained at (a) 17:26, (b) 20:16, and (c) 22:16 UTC.

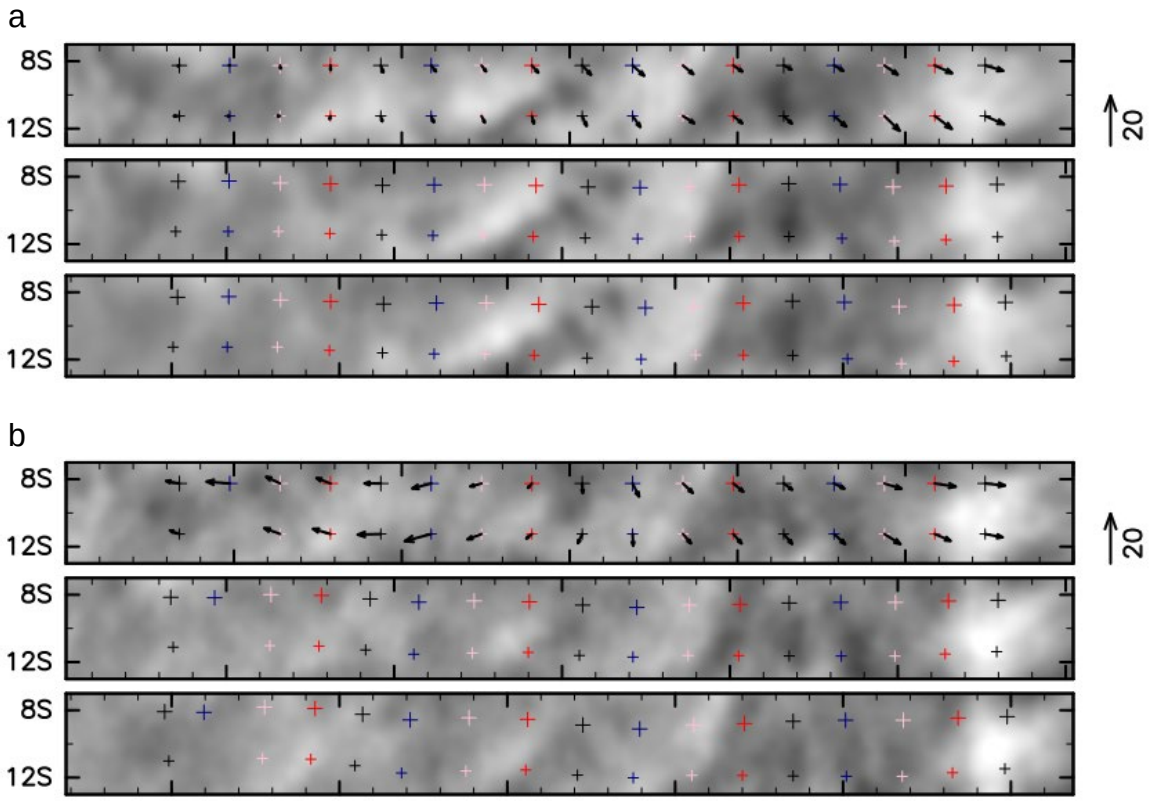

Figure 3: Same as (a) **Fig. 1a-c** (365-nm) and (b) **Fig. 2a-c** (283-nm), but the latitudinal range is limited to 13°S to 7°S for close inspection.

463

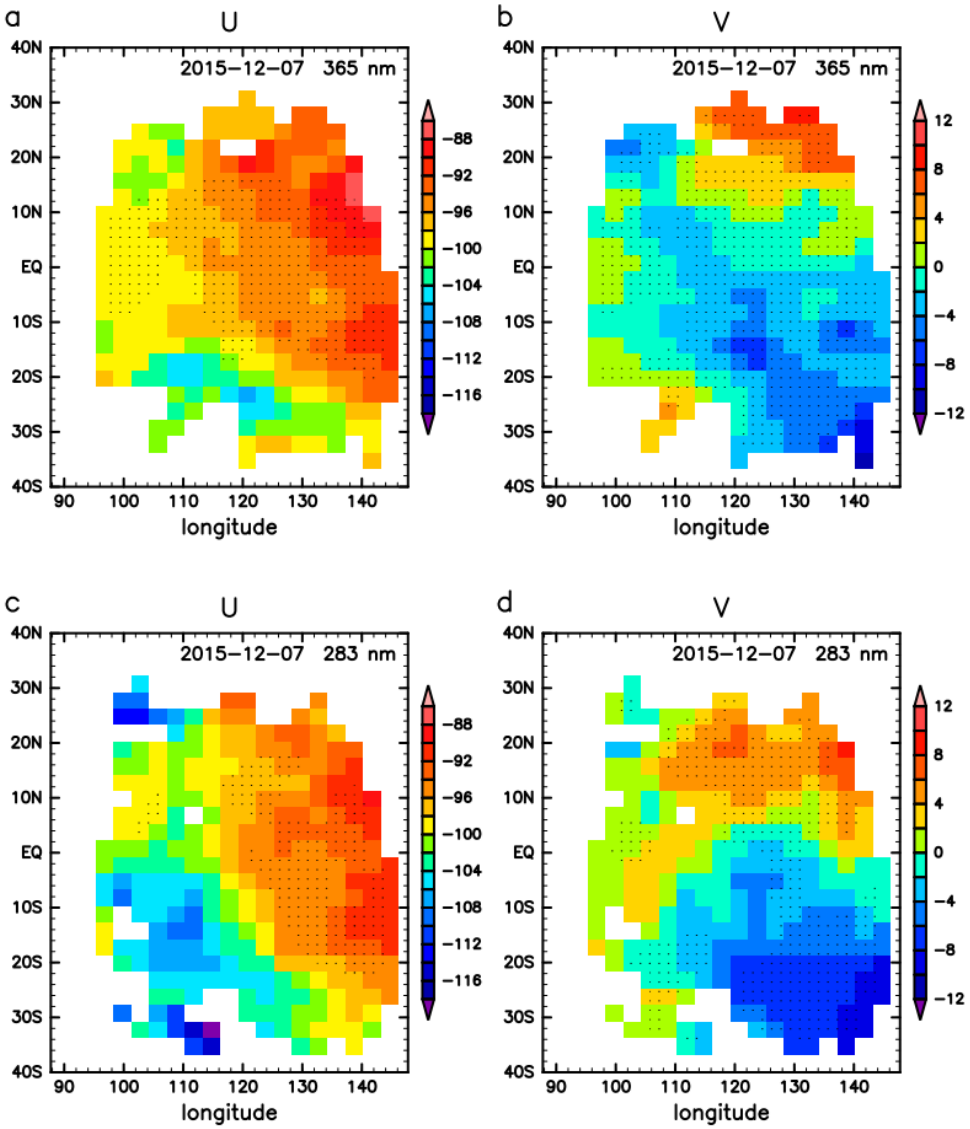

Figure 4: Zonal (a,c) and meridional (b,d) winds obtained by tracking 365-nm (a,b) and 283-nm (c,d) radiance obtained on December 7, 2015. Stipples show where the estimated precision measure ε_u (ε_v) is smaller than 4 m/s for zonal (meridional) winds.

464

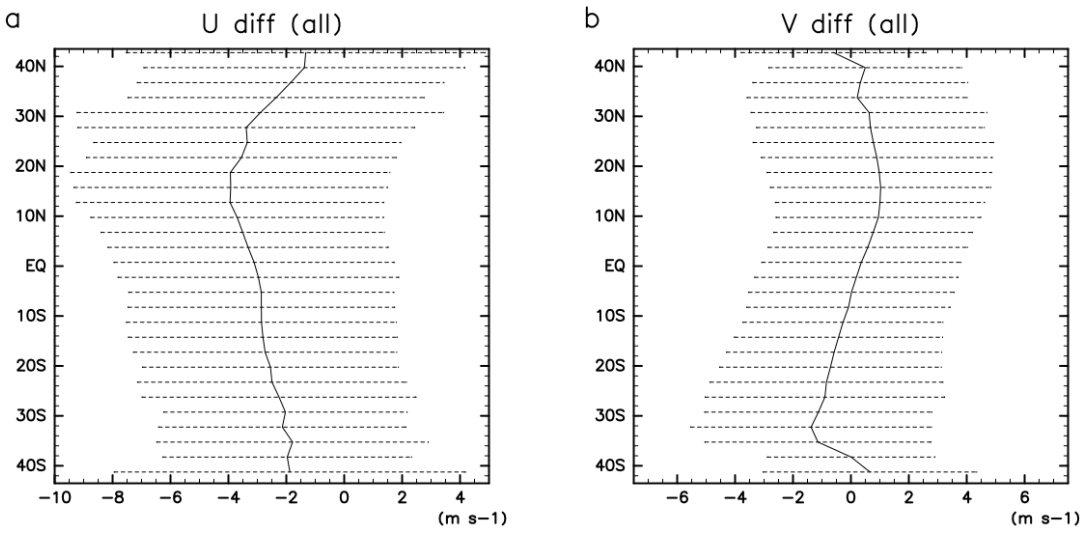

Figure 5: Mean differences in zonal (a) and meridional (b) winds (m/s) between the two UV filters (283-nm results minus 365-nm results) averaged over the observational period (December, 2015 – March, 2017). See the text for the matching condition. The dashed lines show ± the standard deviation at each latitude.

465

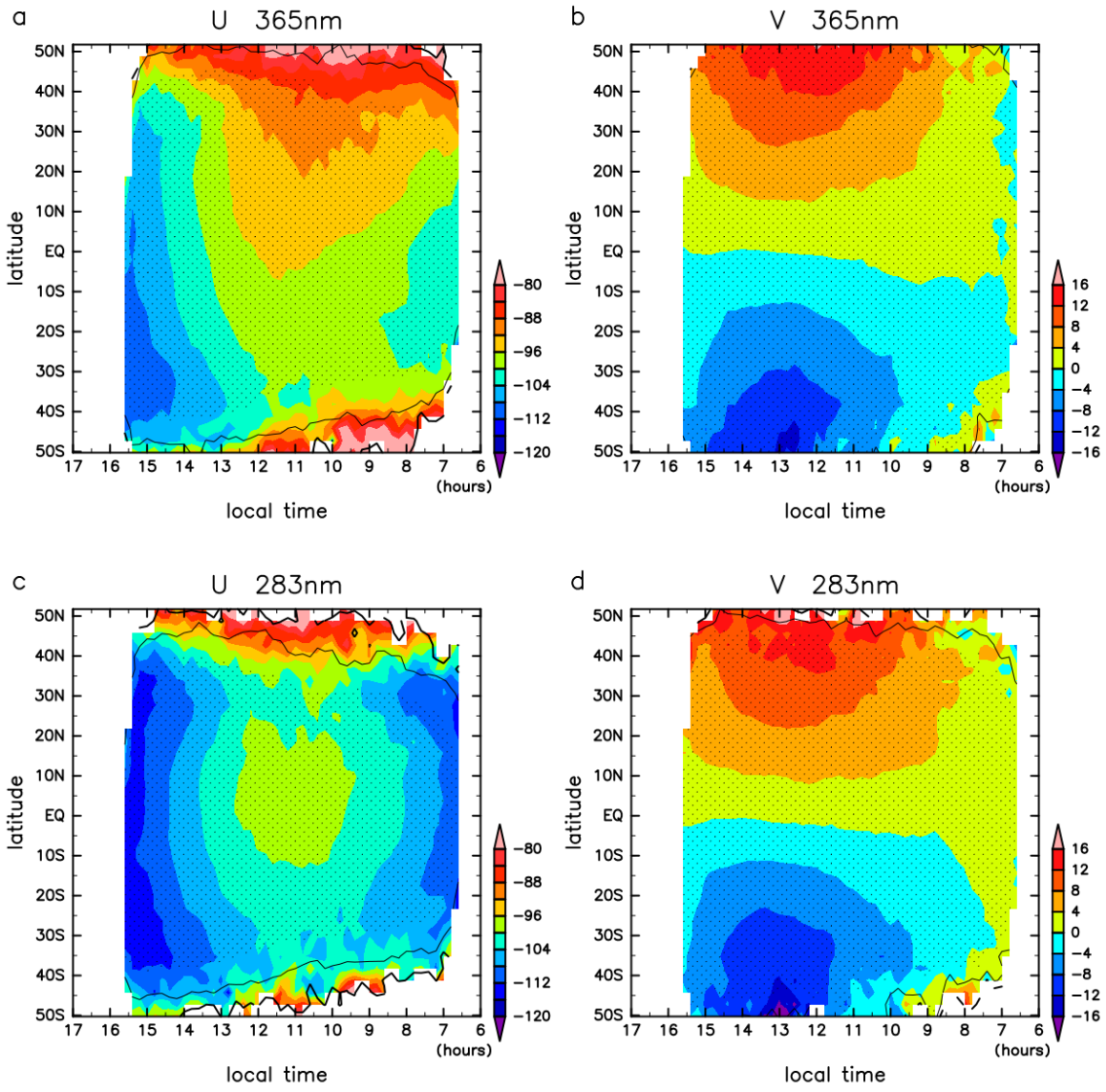

Figure 6: Mean winds obtained as functions of local time and latitude from the entire period (December, 2015 – March, 2017); zonal (a,c) and meridional (b,d) winds from 365-nm (a,b) and 283-nm (c,d) radiance. Stipples show where the indicated precision $\langle \varepsilon_u \rangle$ (a,c) or $\langle \varepsilon_v \rangle$ (b,d) is smaller than 2 m/s. Contours show the same precision measure at 4 and 8 m/s; color-shading is not shown where it exceeds 10 m/s. Note that $\langle \varepsilon_u \rangle$ and $\langle \varepsilon_v \rangle$ do not include any effect from sampling biases (see the text). Local time (abscissa) is shown in the descending order to preserve the longitudinal direction (east to the right).

466

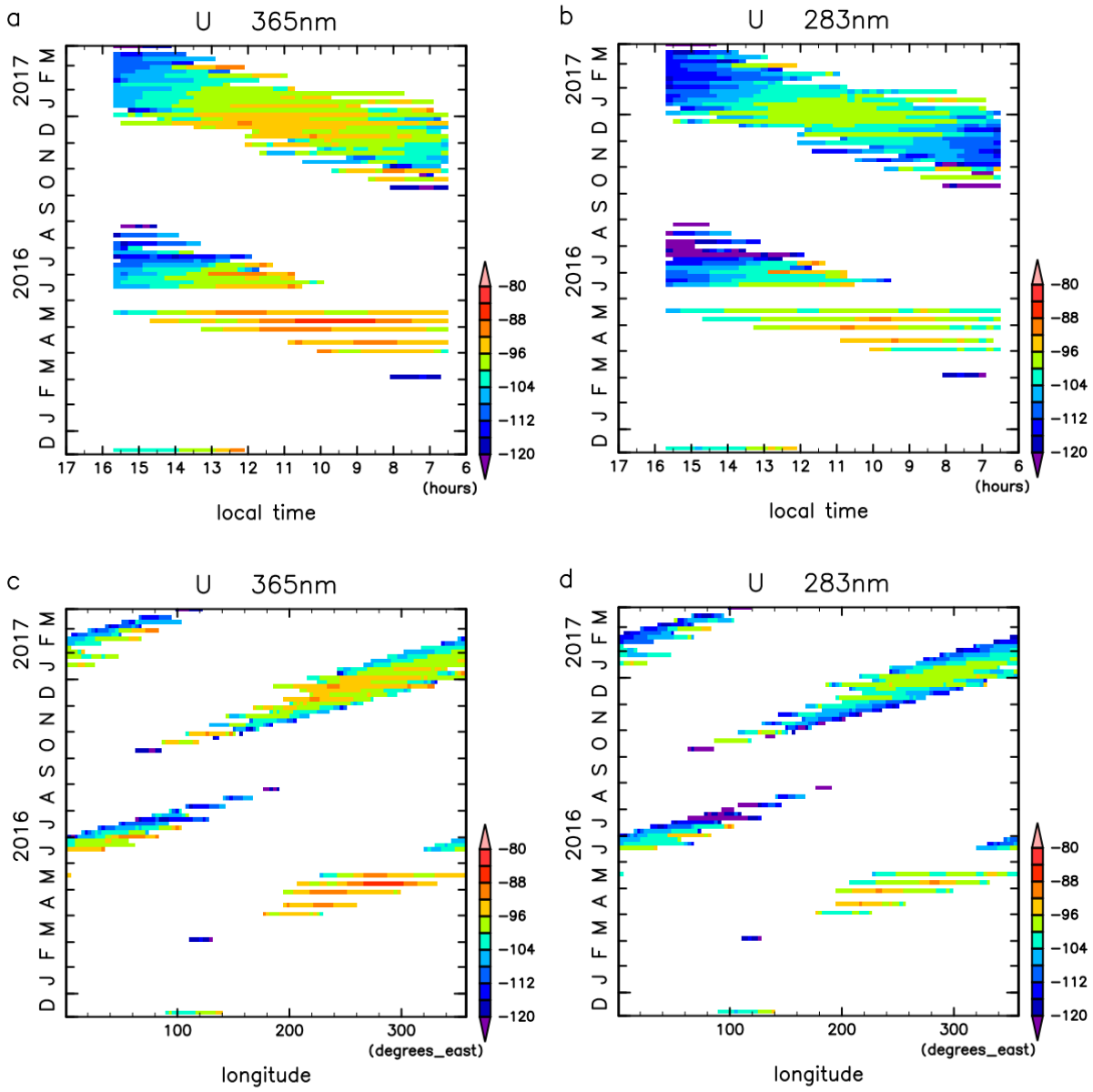

Figure 7: Mean zonal winds between 20°S – 20°N averaged over each of 5-day bins as functions of local time (a,b) and longitude (c,d) from 365-nm (a,c) and 283-nm (c,d) images (m/s). For a given 5-day bin and local-time / longitudinal grid point, the mean value is defined whenever daily-averaged wind values are defined on any day in the 5-day period somewhere between the latitudinal range, so sometimes the representativeness is quite limited.

467

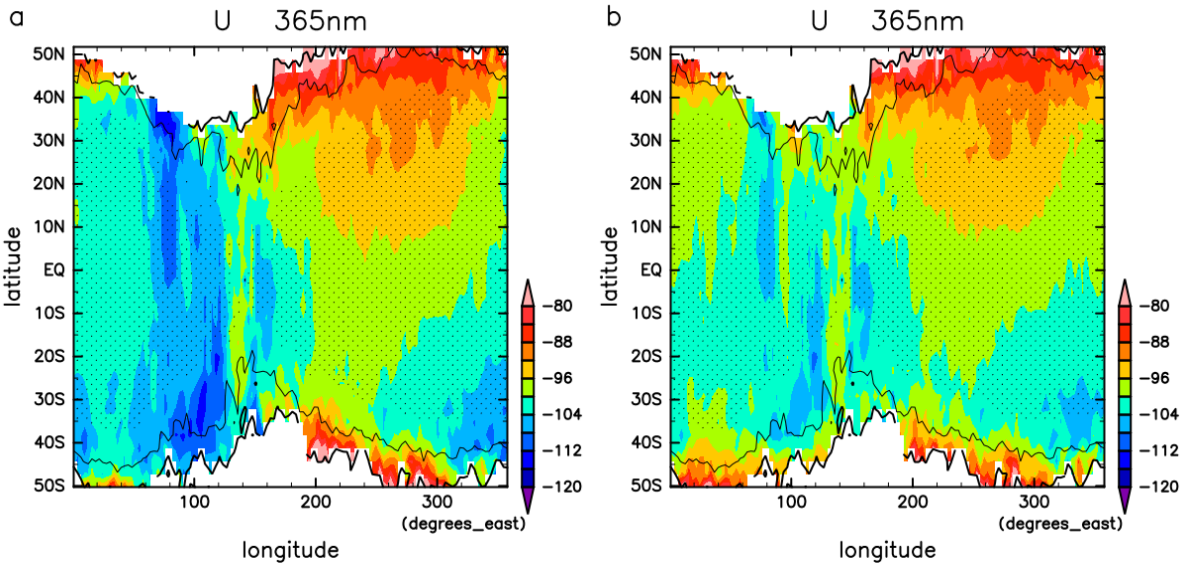

Figure 8: (a) As in **Figure 6a** but obtained as a function of longitude and latitude.

(b) As in (a) except that the local time dependence is subtracted.

468

Availability of data and materials

Radiance data from Akatsuki's cameras will be available publicly from the Akatsuki project's data publication site http://darts.isas.jaxa.jp/planet/project/akatsuki/, and NASA's Planetary Data System (https://pds.nasa.gov/): Atmospheres Node. The first data release is scheduled in 2017.

Competing interests

The authors declare that they have no competing interests.

Authors' Contributions

TH derived conducted cloud tracking, analyzed derived winds, drew figures, and wrote the paper. YJL interpreted the wavelength dependence. TK, TI, KN, MT and JP contributed to the interpretation of derived winds, thermal tides, and mean wind statistics. SM, KO, and TH developed the cloud tracking program, and TK advised it. MT, KO, SM, and TK developed the geographic mapping program for Akatsuki's image data. SM conducted Akatsuki image data processing. AY, MY, and SW developed and calibrated UVI.